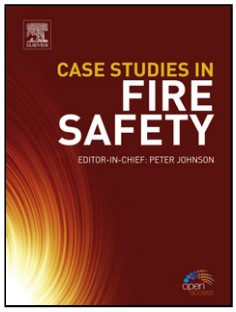

The Role of Niobium Carbides in the Localised Corrosion Initiation of 20Cr-25Ni-Nb Advanced Gas-cooled Reactor Fuel Cladding

Ronald N. Clark, Justin Searle, Tomas L. Martin, W.S. Walters, Geraint Williams

PII: S0010-938X(19)31649-X

DOI: https://doi.org/10.1016/j.corsci.2019.108365

Reference: CS 108365

To appear in: *Corrosion Science*

Received Date: 8 August 2019

Revised Date: 31 October 2019

Accepted Date: 25 November 2019

Please cite this article as: Clark RN, Searle J, Martin TL, Walters WS, Williams G, The Role of Niobium Carbides in the Localised Corrosion Initiation of 20Cr-25Ni-Nb Advanced Gas-cooled Reactor Fuel Cladding, *Corrosion Science* (2019), doi: https://doi.org/10.1016/j.corsci.2019.108365

The Role of Niobium Carbides in the Localised Corrosion Initiation of 20Cr-25Ni-Nb Advanced Gas-cooled Reactor Fuel Cladding

Ronald N. Clark[a1] Ronald.clark@uknnl.com, Justin Searle[b] j.r.searle@swansea.ac.uk, Tomas L. Martin[c] tomas.martin@bristol.ac.uk, W. S. Walters[d] steve.walters@uknnl.com, Geraint Williams[e] geraint.williams@swansea.ac.uk

(a) National Nuclear Laboratory, Building 102B, Stonehouse Park, Sperry Way, Stonehouse, Gloucestershire, GL10 3UT

(b) SPECIFIC IKC, College of Engineering, Swansea University, Baglan Bay Innovation Centre, Central Avenue, Baglan, SA12 7AX, Wales, UK

(c) Interface Analysis Centre, School of Physics, University of Bristol, HH Wills Laboratory, Tyndall Avenue, Bristol BS8 1TL, UK

(d) National Nuclear Laboratory, Building D5 (first floor), Culham Science Centre, Abingdon, Oxfordshire, OX14 3DB

(e) Materials Research Centre, Swansea University, Bay Campus, Fabian Way, Crymlyn Burrows, Swansea, SA1 8EN, Wales, UK

Corresponding author: Ronald Clark, Ronald.clark@uknnl.com

[1]Present address: National Nuclear Laboratory, Building 102B, Stonehouse Park, Sperry Way, Stonehouse, Gloucestershire, GL10 3UT

Graphical abstract

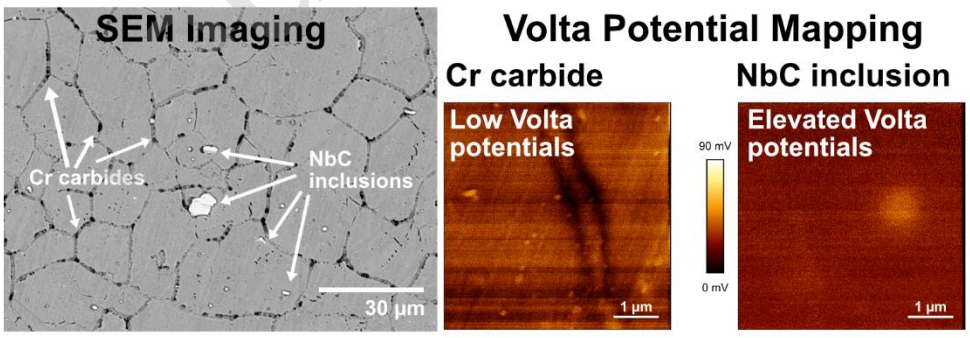

Highlights:

- SKPFM highlights nobility of niobium carbides
- Evidence of intergranular pitting corrosion at niobium carbide inclusions
- EC-AFM provides evidence that intergranular pits form around inclusions

Abstract

The role of niobium carbide (NbC) inclusions in directing the initiation of localised corrosion in sensitised 20Cr-25Ni-Nb stainless steel is investigated using a range of in-situ scanning techniques, allowing visualisation of corrosion behaviour over multiple length scales. Volta potential mapping shows NbC inclusions are up to 30 mV noble to the matrix, while chromium-depleted grain boundaries are up to 65 mV less noble. Corrosion initiation, shown by scanning vibrating electrode technique to comprise highly localised anode sites, is observed at grain boundaries, adjacent to the location of NbC inclusion clusters which remain unaffected by anodic dissolution of the surrounding matrix.

Keywords: Stainless steel A; AFM B ; SEM B; Intergranular corrosion C; Pitting corrosion C; Inclusion C

1. Introduction

Enriched uranium dioxide nuclear fuel from the UKs advanced gas-cooled reactors (AGRs) is clad within a bespoke grade of austenitic stainless steel, herein referred to as 20Cr-25Ni-Nb (Table 1). Following its use in a reactor, spent nuclear fuel is stored within specially engineered water ponds for periods up to several decades as a monitored, retrievable storage regime, pending geological disposal [1]. During in-reactor service, radiation induced segregation (RIS) can occur under specific temperature and neutron flux conditions, leading to significant chromium depletion at grain boundaries [2, 3]. Fast neutron irradiation of the 20Cr-25Ni-Nb crystal lattice leads to displaced atoms (interstitials) and formation of mobile point defects such as vacancies [4]. These defects in-turn diffuse to grain boundaries, exchanging their position with other atoms (inverse Kirkendall effect [5]). Faster diffusing atoms (Cr, Fe) diffuse away from the grain boundary, causing depletion of these elements. Ni, a slow diffusing element by comparison, becomes enriched at the grain boundary. As such the depletion of Cr at grain boundaries renders the stainless steel sensitised and thus

prone to localised intergranular corrosion (IGC). Typically, a minimum of 12 wt. % [Cr] is required for a stainless steel to form a non-porous, invisible, nano-scale, self-healing, protective film (passivation) [6]. Whilst the microstructural effects of various proposed RIS mechanisms have been modelled [7, 8, 9], experimental corrosion investigation of neutron irradiated material is typically limited due to the post-exposure radioactive nature of the stainless steel.

An alternative method is to induce sensitisation through thermal processing [6, 10], whereby chromium (Cr) becomes depleted at regions adjacent to the grain boundaries through the nucleation and growth of Cr carbides. Compared to sensitisation induced in-reactor, such a process produces a wide, >30 nm, Cr depleted zone (with reactor specimens the Cr depleted zone is much narrower, 5-15 nm) [11]. The free carbon levels in as-received 20Cr-25Ni-Nb is low, which is owed to niobium carbide (NbC) precipitates, which form during production when the melt solidifies [12, 13, 14]. High temperature annealing causes incomplete dissolution of NbC, increasing the carbon in solution, and grain growth. Moss and Sykes [14] required temperatures of 1050 and 1150 °C to dissolve the NbC intermetallic. Jones and Ralph [13] performed the solution heat treatment on 20Cr-25Ni-Nb at 1300 °C for 1 hour, which was then cold rolled (10% thickness reduction), and followed this with ageing at 930 °C for 10 hours, their samples were then annealed at higher temperatures for short periods of 1 to 4 minutes at temperatures between 1100 and 1300 °C. NbC particulate size distributions were then recorded using carbon extraction techniques; a 2 minute treatment at 1300 °C was found to have completely dissolved all NbC particles.

Following a high temperature solution anneal the microstructure can be subjected to a lower temperature thermal ageing process resulting in a sensitised microstructure comprising both small scale grain boundary mixed metal (M_6C, $M_{23}C_6$) carbides, alongside larger persistent NbC precipitates. The $M_{23}C_6$ mixed metal carbides (formed by the reaction between Cr, Fe and C (with concentrations of approximately [Cr] ~ 16, [Fe] ~ 7, C ~ [6])) nucleate mainly at grain boundaries, and are composed mainly of Cr, as Cr strongly decreases the activity coefficient for C (i.e. it has a high affinity for C) [6] [14]. Growth then occurs due to the fast diffusion of C to the nucleation site, and slower diffusion by Cr (hence controlling the rate of growth) leading to an interface depleted of Cr. Cr depletion does not only occur at the Cr carbide interface but can also occur at the grain boundary itself. At the temperatures relevant to ageing, alloy grain boundary diffusion is quicker than diffusion

within the bulk, and therefore Cr transport can occur along these networks, causing depletion along the boundary itself [14] [15].

The precipitation characteristics of 20Cr-25Ni-Nb have been investigated in the past by Powell et al [12]. Metal carbides, niobium cyanide (Nb(CN)), G-phase (nickel niobium silicide, $Ni_{18}Nb_6Si_7$) and sigma phase (a brittle intermetallic consisting of Fe and Cr), can all be precipitated depending on the temperature and duration of the aging treatment. Powell et al used electron microscopy and energy dispersive X-ray spectroscopy (EDS) to analyse specimens which had been heat treated for periods of up to 15,000 hours. According to Powell et al, at grain boundary regions, $M_{23}C_6$ will precipitate after 200 hours, G-phase after 500 hours, and sigma phase after 1000 hours. Within the matrix Nb(CN) will precipitate after 200 hours, followed by G-phase and sigma phase after 10,000 hours. Although the stabilising effect of Nb has been studied in the past [16], the effect of these NbC precipitates on corrosion behaviour is not clear. Recent research on this material in open literature has focussed on irradiation effects [17] [18] [19], thermal processing [20] [21] [22], the use of novel corrosion techniques [23], evaluating the alloy in conditions relevant to a pond storage environment [24] [25] [26] [27] [28], dry storage [29] [30], and final geological disposal [31]. Some investigators have undertaken research at a more fundamental level, to assist in establishing the corrosion mechanism [32] [33]. Phuah [32] showed evidence of pitting corrosion around the periphery of NbC inclusions in the 20Cr-25Ni-Nb alloy. Chan et al [33] also observed pitting around NbC inclusions in the alloy, both suggesting that NbC precipitates could be cathodically active, leading to dissolution of the surrounding matrix.

This investigation utilised thermally sensitised 20Cr-25Ni-Nb as a convenient analogue to reactor sensitised material, to elucidate the role of the persisting NbC precipitates in directing the initiation of localised corrosion. To allow observation of corrosion over practical timescales, specimens were in this study were investigated at significantly higher chloride ion concentrations than would be encountered under fuel storage pond environments. The approach utilised by the authors was to use techniques across the length scales. First, a high resolution, non-destructive technique, scanning Kelvin probe force microscopy (SKPFM) was used to map the surface to identify locations which were susceptible to corrosion initiation (approximate length scale ~100 nm – 10s of µm). Second, an in-situ electrochemical scanning vibrating electrode technique (SVET) was then employed to obtain spatially resolved current density maps (approximate length scale ~100s of µm).

Third, time lapse techniques were then employed (optical time lapse microscopy 'TLM' and electrochemical atomic force microscopy 'EC-AFM') which provided visual confirmation on the initiation and propagation of localised corrosion (approximate length scale ~100s μm, ~100 nm - 10s of μm). By utilising this multiscale approach, combined with scanning electron microscopy (SEM) and focussed ion beam scanning electron microscopy (FIB-SEM) methods to analyse both pre- and post-corrosion surfaces, the sites of corrosion initiation could be pinpointed. A notable aim of this work was to clarify the role of NbC inclusions on IGC initiation. Past work by Phuah et al [32] and Chan et al [33] has shown evidence of localised corrosion at NbC inclusion sites, and it has been suggested that NbC inclusions form a micro galvanic couple with the austenite matrix. Corrosion site mapping using SKPFM will assist in evaluating the micro galvanic coupling hypothesis suggested by previous investigators. In this study a combination of in-situ and ex-situ techniques across multiple length scales has been used to give additional insight into localised corrosion.

2. Experimental

Material and Thermal Processing

Sample material, 20Cr-25Ni-Nb stainless steel, was sourced as flat strip (350 x 200 x 0.8 mm thickness) from Westinghouse. The name given to the bespoke grade of austenitic stainless steel is taken from its composition. The thermal sensitisation process was conducted as follows:

- solution anneal at 1150 °C for 30 minutes in an argon atmosphere to dissolve NbC, increasing free carbon within the matrix
- water quench to prevent recombination of NbC
- aging treatment at 600 °C for 2 weeks (~336 hours) in air to stimulate nucleation and growth of chromium carbide precipitates at grain boundary locations, thereby causing localised chromium depletion (sensitisation)

Following the thermal sensitisation process the strip was cut by hand guillotine to form ~20 x 20 mm specimens. Where an electrical connection was required a wire was spot welded to the specimen and the specimen mounted in a non-conductive cold set resin (Struers Epofix). Specimens were abraded using SiC paper (P180 – P2500) and subsequently polished to a 1 μm surface finish using diamond suspension. An electrolytic etch was used to reveal the microstructure for the scanning Kelvin probe force microscopy (SKPFM) experiment. This

was conducted by immersing the specimen and a Pt gauze counter electrode in a solution of 10 wt. % oxalic acid and polarising the specimens to 6 V for a period of 10 seconds.

Experimental Techniques

An overview of the experiments conducted is given in Table 2. NaCl solutions were prepared using ACS reagent from Sigma Aldrich. A very high chloride concentration (35,450 ppm or 35.5 $g \cdot L^{-1}$ [Cl^-]) was chosen for the atomic force microscopy (AFM) investigation as the corrosion rate was compatible with the scan time achievable, i.e. corrosion propagation could be followed effectively over the course of a few hours.

A JPK Nanowizard III AFM was used to collect information on topography (AFM), SKPFM and EC-AFM. Low stiffness Nanoworld FM50 AFM cantilevers were used for AFM imaging and SKPFM mapping in non-contact AC mode, whilst triple cantilever silicon tips were used for EC-AFM (Mikromasch HQ:CSC37). To collect a Kelvin probe measurement, an electrical connection was required, which was achieved by attaching copper foil to the specimen outside of the scan area. A raster scan is performed by the SKPFM probe; which collects topographical information and Kelvin potential information line by line. Using feedback from the topography; the probe hovers above the surface at a user defined height (50 nm) when conducting the SKPFM mapping, and as such the recorded potentials are independent of feature height. The values obtained through SKPFM were inverted as per convention (darker areas more susceptible to anodic dissolution). The SKPFM methodology has been compared to the conventional SKP method previously by Rohwerder [34]. In order to reveal the microstructure, the specimens were electro-etched using 10 wt. % oxalic acid for a period of 10 seconds. This etch was performed on as-received specimens only; for sensitised specimens, sensitised grain boundaries were visible without the need for an etch.

A JPK "3-port small volume SmallCell" was used for EC-AFM and the quantity of electrolyte was <60 µL, distributed over a surface area of ~1.8 cm^2. The process followed for EC-AFM was as follows: firstly, a topographic image was recorded using contact mode AFM in air, then the electrolyte was introduced slowly to avoid damage to the AFM tip. Once fully immersed the instrument was reconfigured for measurement under electrolyte, which included compensation for the change in refractive index. It is estimated that ~15 minutes had passed prior to the first scan. Individual scans were performed over a 50 µm area at a scan speed of 0.3 Hz which resulted in a scan time of ~30 minutes. A 512 x 512 pixel

resolution was used, thus each pixel represented 97 nm^2. AFM data post-processing was undertaken by JPK instruments data processing software version spm5.1.4. First order levelling was applied to all data; with the lower 5% and upper 80% being excluded from the fit.

In-situ TLM images were taken using a Meiji MT8000 microscope with an Infinity 1-3C digital camera. Once a suitable area of the specimen was identified, a small strip of PTFE tape (HD5490) was perforated using a 0.5 mm biopsy pen (area exposed ~0.2 mm^2), and subsequently placed onto the surface. Specimens were then fixed on the centre of a large petri dish and immersed in ~300 ml electrolyte ([0.35 $g{\cdot}L^{-1}$ $[Cl^-]$]). In this experiment the objective lens was in contact with the electrolyte, so a waterproof shroud was used as protection. The specimen was studied under potentiodynamic polarisation (Palmsens 3) using a saturated calomel electrode (SCE) and Pt gauze counter electrode both positioned as close as possible to the exposed area. The specimen was polarised from the measured free corrosion potential (E_{corr}, -130 mV SCE) to breakdown potential (Eb, +850 mV SCE).

SVET measurements were undertaken using an instrument of in-house design and construction described in detail elsewhere [35] [36]. The SVET-derived peak to peak voltage was converted to a current density value by means of a calibration procedure employed using a two-compartment cell using the electrolyte of interest, as reported previously [36]. A ~35 mm^2 area of the specimen was masked using PTFE tape (HD5490). Following the calibration procedure ~5 L of NaCl (aq) was used (1 $g{\cdot}L^{-1}$ $[Cl^-]$). A potentiostat (Palmsens 3) was used to apply a potential to the specimen, an SCE reference electrode and Pt gauze counter electrode were used. The specimen was unperturbed at the free corrosion potential for 600 s. The potential was then increased by 50 mV steps from 0 mV_{SCE}. Four SVET scans were performed after each potential step. After the breakdown potential (E_b) had been reached, the experiment was halted, the specimen removed from solution, rinsed with water and subsequently examined by SEM-EDS (JEOL 6010-PLUS). Sectioning was performed using FIB-SEM (FEI Helios NanoLab 600i Dual Beam). Before FIB sectioning, to preserve the subject and surrounding surface from the Ga beam, Pt was deposited prior to cutting. No other surface preparation was performed; to preserve the corroded surface.

3. Results and Discussion

AFM and SKPFM

A scanning Kelvin probe force microscope (SKPFM) was used to determine the Volta potential difference between inclusions and the austenite matrix with respect to the AFM probe. SKPFM has been used in the past to evaluate several different metal systems: Al alloys [37] [38], high-entropy alloys [39], filiform corrosion [40] and Co-Cr-Mo alloys undergoing hot isostatic pressing (HIP) [41].

Figure 1 shows AFM topography and Kelvin potential maps of the austenitic stainless steel in an as-received format. Lighter areas on the AFM topography maps are areas proud of the matrix. Lighter areas in the Kelvin potential maps indicate phases less thermodynamically susceptible to corrosion. The as-received images show the typical blocky NbC inclusions present in the stainless steel (a typical image of the thermally sensitised microstructure is shown in Figure 2), all of which are proud of the matrix. NbC are not only located in the matrix, but adjacent to, and at grain boundaries. The high Volta potentials recorded for the inclusions indicated that they are noble with respect to the matrix, and thus, thermodynamically, less prone to anodic dissolution. Within the as-received material the grain boundaries appear to have a similar Volta potential to the matrix, if not slightly greater. This is repeated in the next set of images, however in comparison to the thermally sensitised specimens this effect is not as significant (Figure 3).

As expected with the thermally sensitised specimens (Figure 3), lower Volta potentials were recorded at the grain boundaries, due to localised Cr depletion at grain boundary locations, caused by the formation of Cr carbides. The Cr carbides are less proud of the microstructure and have a distinctly different shape to that of the Nb carbides, as shown in Figure 2. Not all sensitised grain boundaries had the same thermodynamic susceptibility to anodic dissolution, as Figure 3 shows low Volta potentials along discrete areas of the grain boundary. As has been shown in the past, Tedmon et al. [6] indicate that it is not the size or number of Cr carbides, but the extent of Cr depletion at grain boundary locations that cause sensitisation of stainless steels. At higher ageing temperatures (700 and 800 °C) Tedmon et al. showed that austenitic stainless steel can show evidence of non-uniform attack at grain boundaries i.e. the depletion does not exceed the critical value of 12 wt. % Cr. At 600 °C however Tedmon et al. describe the depleted zones as being ‘very susceptible to attack’, so the grain boundaries in the material shown here should be highly sensitised. Tedmon et al. also indicate another possibility; if the Cr depletion at a location between Cr carbides is highly depleted of Cr (i.e. the concentration drops much lower than the critical Cr value)

then 'patchy' IGC may be expected. This provides some basis for highly localised high Volta potentials shown in the SKPFM maps shown in this paper. The reader should be aware of the differences between the previous and present work: Tedmon et al. conducted their ageing treatment at 600 °C for a period of 24 hours without the need for a solution anneal as no carbide stabiliser was present within their 304 stainless steel alloy with higher C content (0.45 %). As Tedmon et al. mention themselves, greater Cr additions decrease the activity co-efficient for C (easier to form carbides), whilst greater Ni additions act to increase the activity co-efficient of C (more difficult to form carbides), the alloy used in this study has both greater Cr and Ni content compared to type 304. Figure 3(ii and iv) shows highly localised regions of low Volta potential, indicative of highly localised Cr depletion from the sensitisation process. Figure 3(vi) shows a Cr carbide and neighbouring NbC inclusion, which shows that the inclusions remain noble when the material is thermally sensitised.

Time-Lapse Microscopy

Time-lapse microscopy (TLM) is a simple, effective technique for *in-situ* imaging of corrosion on surfaces at the microstructural level [42] [43]. In an accelerated TLM experiment, the thermally sensitised 20Cr-25Ni-Nb specimen was polarised from the free corrosion potential (-130 mV_{SCE}) to breakdown potential (850 mV_{SCE}) and imaged *in-situ*. The breakdown potential was determined by assessing the slope of the potentiodynamic polarisation curve. The excessive change in potential required for breakdown could suggest that there was a low degree of sensitisation. Previous results using conventional sized specimens (exposed areas ~1 cm^2) showed smaller total changes in potential for the same concentration of electrolyte [44]; indicating that this discrepancy in the breakdown potential may be an artefact of the smaller exposed area. The principle is simple: if a smaller area is exposed, the probability of having a susceptible site for corrosion initiation is decreased, and hence higher potentials may be required for corrosion initiation. TLM stills are shown in Figure 4. Intergranular corrosion (IGC) initiated at a grain boundary intersection. Chan [33] also witnessed IGC initiation at grain boundary intersections, under potentiodynamic control (-200 to +1000 mV_{OCP}, 500 ppm [Cl^-]), corrosion then continued to propagate along grain boundaries, but appeared pit-like, resembling intergranular pitting corrosion [45]. The grain boundaries were subjected to localised corrosion, along with the formation of a lacy cover. Once loss of passivity occurs, due to the absorption of ions, or thinning of the passive film, metastable pitting can occur, and subsequently metal oxidation causes the formation of

metal cations, in turn leading to electromigration of the Cl^- anion toward the pit to maintain charge neutrality, and hence becomes an autocatalytic process. For 300 series austenitic stainless steel past work has indicated that there is a critical threshold for pit stability; which for pit propagation, requires a solution of greater than 70% saturated metal chloride [46] [47]. In such environments the pit solution can become supersaturated, leading to the precipitation of an iron (II) (ferrous) chloride film, often at the bottom of the pit. The pit chemistry can be extremely acidic, and in some cases the pH can be less than zero, and [Cl^-] much greater than the bulk [48]. The lacy pit covers act to both limit transport of species to and from the pit, thereby maintaining the aggressive conditions, compared to the bulk chemistry, favouring propagation. Figure 5 shows crops of the images, which highlight a ~3 µm NbC inclusion (highlighted by the red arrow) which, in agreement with the earlier SKPFM study, remains immune to anodic dissolution, compared to grain boundaries which were susceptible to IGC.

Scanning Vibrating Electrode Technique

In-situ scanning vibrating electrode technique (SVET) visualisation of localised corrosion in the absence of external polarisation (E_{corr} = -480 mV_{SCE}) and within an applied potential range up to +650 mV_{SCE} showed no evidence of passivity breakdown. However, when the potential was increased to +700 mV_{SCE}, breakdown of the passive film occurred, and several highly focal anode sites were detected on the exposed surface with associated local current density values in the range +20 to +80 $A{\cdot}m^{-2}$ (Figure 6). The time between the images is ~12 minutes, and in total the experiment lasted 4 hours and 33 minutes.

Williams and McMurray [35] conducted SVET experiments on freely corroding 11.5 wt. % Cr stainless steel in 0.6 to 5 $mol{\cdot}dm^{-3}$ NaCl (aq), which corresponds to ~14 to ~177 $g{\cdot}L^{-1}$, (SVET experiments in the present paper used a lower [Cl^-][1]). Williams and McMurray observed that 1-2 stable pits per cm^{-2} were detected at concentrations less than 2 $mol{\cdot}dm^{-3}$ (70 $g{\cdot}L^{-1}$), whereas at greater [Cl^-] (>4 $mol{\cdot}dm^{-3}$) the number of stable pits detected increased (to 4-5 pits per cm^{-2}). In comparison, in this experiment several pits initiated, and remained active throughout, however one of the pits showed a noticeable change in current density with

[1] The highest [Cl^-] used in the present paper was for the EC-AFM study (35.5 $g{\cdot}L^{-1}$), the SVET and TLM studies used 1 $g{\cdot}L^{-1}$ and 0.35 $g{\cdot}L^{-1}$ respectively

time, appearing to have passivated. The anode at site D initiated early in the experiment, however struggled to compete with nearby anodic sites, despite the greater current density at this location compared to anode C. Figure 7 shows the increase in current density at anode site C, and consequent diminishing current density at anode site D with changing exposure time. The figure also shows author estimated current densities for two of the scans which were topped out (4 h 11 m and 4 h 16 m).

Using a similar electrochemical scanning technique (scanning reference electrode technique (SRET)) Isaacs showed on type 304 stainless steels [49] that many pits initiate, typically however most repassivate and a single pit becomes prevalent. The large free surface on the stainless steel effectively becomes a net cathode as to compensate for the charge at the highly localised anodic current sources. Previous studies by Williams et al. show a similar effect in the pitting of magnesium using SVET [36]. As with most instruments there is a compromise between measurement sensitivity and measurement range. In this experiment the recorded current density had reached a maximum as a result of the high sensitivity setting; therefore, the true current densities recorded will have been much greater (as shown in the estimates in Figure 7). Given that the specimen was polarised no regions of cathodic activity are shown in the current density maps, as cathodic activity would have been occurring at the counter electrode.

SVET Post Corrosion Imaging and Elemental Analysis

Following the experiment, the specimen was investigated using scanning electron microscopy (back scatter electron detector utilised) in conjunction with EDS for elemental analysis. Imaging revealed the presence of intergranular pitting corrosion. The principal sites of anodic dissolution detected by SVET appeared to be pit-like in nature, resembling intergranular pitting corrosion. EDS mapping showed an abundance of Nb-rich precipitates at each of the anodic sites. Example images are shown for the intergranular pits at sites B (Figure 8), D (Figure 9), and G (Figure 10). The results from site B are typical of the specimen (Figure 8); other pit sites also showed the presence of a high number of Nb-rich precipitates, while regions distant from these pits saw no Nb-rich particulate clustering. The backscatter electron images showed the presence of a lacy cover, as witnessed with the TLM experiment, but also the presence of numerous Nb-rich precipitates, which appear brighter due to the different atomic number. The example images are each complimented by EDS

false colour maps, showing the extent to which Nb-rich particulates are associated with pit sites. Higher magnification images showed that within the pit itself, Nb appears to be much more finely dispersed. Several of the Nb-rich precipitates were surrounded by a dark halo, resembling a shadow, and it is postulated that these Nb-rich precipitates may have been expelled from the pits during the experiment. Using *in-situ* high-speed atomic force microscopy (HS-AFM) Laferrere et al. [23] imaged the corroding microstructure of thermally sensitised 20Cr-25Ni-Nb material, and in their experiment showed the removal of Cr carbide precipitates from the grain boundary, whist the specimen was under potential control. Moore et al [50] went further and showed how data from HS-AFM, alongside SEM and FIB milling, could be used to model localised grain boundary dissolution on sensitised 304 stainless steel in NaCl. Complimentary to the previous work, the grain boundaries of the specimens here show evidence of carbide removal from the grain boundary; caused by oxidation of the adjacent Cr-depleted volume. As with the Figure 8, Figure 9 shows the association of Nb-rich precipitates with the intergranular pit at site D. In this figure the Cr carbide removal from grain boundaries is easily seen; interestingly both at the oxidised grain boundary and within the lacy cover there is evidence of Nb enrichment.

Figure 10 shows the intergranular pit at site G, which shows a pit without a lacy cover present on the left, and a pit with a lacy cover present on the right. Also included is a higher magnification image within the pit marked by the purple arrow in Figure 10(i), which shows the presence of several NbC inclusions within the pit (Figure 10(ii)). The larger blocky inclusions are also surrounded by several finer bright particulates, assumed to also be NbC. The larger inclusions (~3-4 µm) do not appear to show any signs of corrosion, and evidence that again supports the earlier SKPFM mapping and TLM experiments. Figure 10(iii) shows an area where Cr carbides once decorated the grain boundary, and again the extent of Nb-rich particulate clustering that has been observed with other the intergranular pits. Once again there is the association of Nb-rich particulates within the holes of the lacy cover itself. These examples indicate that whilst NbC may not be prone to dissolution they appear to play a role in directing IGC initiation where clusters of NbC are present.

Following post corrosion imaging using SEM, the specimen was analysed using a higher resolution FIB-SEM ('dualbeam') instrument with EDS capability. This allowed higher magnification imaging, and the ability to perform sectioning of NbC inclusions. Unfortunately, between imaging using the SEM and FIB-SEM the lacy covers were removed.

The FIB-SEM instrument used had the ability to tilt the specimen and therefore afforded a different perspective of the surface. Figure 11 shows an example intergranular pit site using secondary electron imaging (note the change of imaging mode). By tilting the specimen it was discerned that the earlier 'dark halos' observed around NbC in the earlier micrographs were likely due to the NbC sitting on the surfaces outside the pit. This is further evidence that the NbC are noble with respect to the surrounding matrix and Cr-depleted grain boundaries. Whilst it is possible that the NbC act in directing the corrosion of the surrounding metal by a micro-galvanic coupling effect, this more recent analysis areas directly surrounding the NbC inclusions showed no evidence of localised corrosion. Figure 12 secondary electron imaging shows an oxidised grain boundary with an NbC inclusion present, before (Figure 12(i)) and after sectioning (Figure 12(ii)). The images show how the inclusion was still present, despite the corrosion present subsurface. The particle directly behind the NbC inclusion was analysed by EDS, which confirmed that it was rich in Al and O, therefore it was expected that it arose from the sample preparation procedure.

EC-AFM

Figure 13 shows a series of *in-situ* AFM measurements on a thermally sensitised 20Cr-25Ni-Nb specimen following immersion in 1 mol dm^{-3} NaCl (aq) (35.5 $g \cdot L^{-1}$ $[Cl^-]$) over the period of 4.5 hours in freely corroding conditions. A total of nine images were collected, with each image taking ~30 minutes to collect. Shown are scans (i) 30 minutes, (ii) 1 hour, (iii) 1 hours 30 minutes, (iv) 2 hours, (v) 2 hours 30 minutes, (vi) 4 hours. The apparent swelling effect witnessed at grain boundaries, which becomes more prominent in the later images, is expected to be a visual artefact caused by the relative height scale used. Localised pitting events initiated quickly on the surface, the first of which initiated along a sensitised grain boundary adjacent to a particle near the centre of the frame within the first image (shown by arrow in Figure 13(i)). It is expected that this is an NbC inclusion, given the resistance to corrosion throughout the experiment, in agreement with the earlier SKPFM mapping, TLM, and SVET experiments. Phuah [32] witnessed similar results after potentiodynamic polarisation of thermally sensitised 20Cr-25Ni-Nb, NbC remained intact despite pits forming around them, leading to the hypothesis that NbC may form a galvanic couple with the matrix, with the surrounding metal acting as a sacrificial anode. Bai et al. [51] saw that Nb(C,N) inclusions, present in super 304H stainless steel, were resistant to corrosion, and

had no direct link to pit initiation. Generally N has a positive impact on pitting resistance [52] [53], thus Bai et al. attribute corrosion witnessed at these locations to be the result of the reduced [N] available in the matrix (as Nb(C,N) had precipitated). The majority of the localised pitting corrosion events had occurred after ~1 hour immersion (Figure 13(ii)); and notably a pit cover formed around the inclusion. By the following image (Figure 13(iii)) the pit cover was removed, possibly by the AFM tip itself. In an AFM experiment Zhang et al. [54] witnessed the removal of a pit cover on sensitised 304SS in 3.5 Wt.% NaCl; once the pit cap was removed, the pit ceased to propagate. For the stainless steels to passivate, the surfaces form an invisible Cr-oxide film; however as has been discussed previously, IGC can occur once [Cr] drops below a critical threshold. Of the pits visible within the scan area four out of five nucleated adjacent to a grain boundary. It is expected that these pits initiated at these locations because of highly localised differences in Volta potential, as shown by SKPFM, possibly caused by inhomogeneous Cr depletion along the grain boundary. As has been discussed earlier, pit covers provide protection, thereby assisting in pit stability [55]. The lacy cover impedes mass transport, maintaining the aggressive environment and thus enabling pit propagation. There was a distinct increase in what appears to be noise by Figure 13(v) at 2 hours 30 minutes, and increased further in Figure 13(vi), which made it difficult to make out features. To assess the noise; a smaller working area, 20 μm^2, was selected in the centre of frame and a higher setpoint used (image not shown). Typically false lines can appear on AFM maps when the set point and gains are not optimised, causing the probe trace and retrace to not follow each other. In this experiment, both lines showed agreement. Though the traces matched, features from one line did not necessarily follow on the next line, indicating removal of features has occurred. It is expected that this is caused by weakly adherent Fe (II, III) oxide corrosion products being moved by the AFM tip. The lack of pit propagation may be due to insufficient chromium depletion at grain boundaries, owing to insufficient carbon in solid solution following the high temperature anneal.

Discussion

Whilst the experiments and analysis performed within this paper do not provide a definitive indication of the site for IGC initiation, they provide useful information to assist in understanding the mechanism for corrosion on this thermally sensitised stainless steel. SKPFM mapping provided an indication on the thermodynamic susceptibility of phases

within the stainless steel to corrode. The mapping predicted that NbC inclusions would be noble with respect to the matrix, and that both the Cr carbides and the directly surrounding areas would be less noble than the matrix. The mapping also showed that, with the specimens used, Cr depletion appeared highly localised, along different sections of the grain boundary. Subsequent *in-situ* experiments using both TLM and SVET showed that NbC appeared to be unaffected during corrosion, whilst the grain boundaries, containing Cr carbides, were oxidised preferentially. In post corrosion imaging, following the SVET experiment, NbC inclusions were present on the surface without showing any signs of oxidation, as though they had been removed from the pits and settled on the free surface. There was evidence of localised corrosion of the Cr depleted volumes present around Cr carbides, shown by small pits on grain boundaries, in agreement with Laferrere et al. [23]. EDS analysis showed that intergranular pits were abundant in Nb, evidence that corrosion is linked to areas where a high number density of Nb-rich precipitates were present. In one example the pit mouth showed a fine dispersion of Nb precipitates, and in another there was a high density of precipitates. Areas away from the pits showed less Nb-rich precipitate clustering. In order to investigate further, FIB-SEM sectioning was performed on an NbC inclusion present at an oxidised grain boundary, in close vicinity to one of the intergranular pit sites. Whilst oxidisation along the grain boundary was present, areas adjacent to the inclusion showed no evidence of localised corrosion, however there was considerable excavation present subsurface (confirming that NbC particles are noble). The EC-AFM experiment provided a closer view of what was occurring at the grain level, where the majority of intergranular pits initiated at grain boundary locations but passivated before gross corrosion occurred. One pit initiated at a grain boundary intersection in close vicinity to a precipitate, expected to be NbC; this continued to propagate until the pit cover was removed, thought to be due to the AFM tip. The NbC inclusion remained intact throughout the experiment, again supporting evidence for nobility of this phase. Phuah [32] indicated that the surrounding areas around NbC inclusions may suffer from anodic attack due to the formation of a micro galvanic couple, due to the nobility of the NbC phase, and that these small secondary phases are critical to corrosion. The SKPFM work reported in this paper, that NbC inclusions are cathodic with respect to the matrix and Cr-depleted grain boundaries, supporting the literature. Chan [33] similarly indicated that “Nb-rich precipitates play an important role in the corrosion process”, from post corrosion imaging

work, where pits were witnessed around Nb precipitates in a stabilised 20Cr-25Ni-Nb microstructure. Indeed, post corrosion imaging by this author (Figure 14) following potentiodynamic polarisation in 0.35 $g \cdot L^{-1}$ [Cl^-] showed the formation of pits around NbC inclusions on unsensitised 20Cr-25Ni-Nb. The present TLM, SVET, post corrosion imaging, and more in-depth analysis by FIB-SEM sectioning do not definitively provide proof of localised corrosion initiation around these inclusions. That said, it is possible that during the early stages of intergranular pit formation in the SVET experiment that corrosion had initiated at regions along sensitised grain boundaries in close vicinity to NbC inclusions (such as was witnessed in the EC-AFM experiment) and in Figure 14. The SVET post corrosion imaging and EDS analysis did however reveal that at each intergranular pit site Nb-rich precipitates were in high abundance, indicating that such increased Nb-rich precipitate density regions are linked to corrosion initiation.

4. Conclusions

The addition of Nb as a stabiliser in 20Cr-25Ni-Nb stainless steel is required to sequester carbon, thus reducing susceptibility to thermal sensitisation. Although not conclusive, this study provides useful evidence that NbC inclusions, observed in both as-received and thermally sensitised material, play a role in the initiation of localised corrosion of this stainless steel. It is proposed that these clusters of particles form preferential anodic metal dissolution sites, creating initiation points for IGC. As such these results provide evidence to support previously published theories: such as micro-galvanic coupling between NbC-austenite [33] [32], and nitrogen depletion around Nb(C,N) on localised corrosion behaviour [51].

In order to provide further the knowledge in this area, a correlative tomography approach, similar to that undertaken by Burnett et al could be used [45]. In-situ synchrotron X-ray tomography [56] [57], and in-situ high-speed AFM [23] [50] [58], could be employed together as complimentary techniques. High-speed AFM, due to its high temporal and spatial resolution, would be able to provide very detailed information on the early stages of corrosion initiation around the sensitised grain boundaries and these NbC inclusions. X-ray tomography is unique in that it can provide a three dimensional view of the corroding material, though in comparison has a much smaller temporal resolution, even when using

synchrotron-based X-ray sources [57] (voxel sizes are in the order of 0.1-1 µm [56]). As such, in-situ synchrotron X-ray tomography would likely only be able to provide information on corrosion propagation around NbC inclusions larger than at least a micron. High-speed AFM would be suited to capture information on the very early stages of corrosion initiation, whilst the use of X-ray tomography would allow the later stages of initiation and propagation of corrosion to be followed on the larger length scale.

The combination of multi length scale techniques (SVET, TLM, EC-AFM), high resolution material characterisation (AFM, SKPFM) and a subsurface ion/electron microscopy technique (FIB-SEM) employed herein therefore provide an insightful means of characterising corrosion initiation sites in a key alloy system for the nuclear industry.

Data Availability Statement

The raw data required to reproduce these findings are available to download from [INSERT PERMANENT WEB LINK(s)]. The processed data required to reproduce these findings are available to download from [INSERT PERMANENT WEB LINK(s)].

Declaration of interests

There are no known conflicts of interest.

Acknowledgements

We would like to acknowledge the Nuclear Decommissioning Authority for providing PhD funding and the National Nuclear Laboratory for providing Leading Science and Innovation funding. Westinghouse are thanked for supplying the sample material.

References

[1] Nuclear Decommissioning Authority, “Position Paper of NDA Research Board / NDARB2016, Review of NDA's Spent Fuels R&D Programme, Issue 1,” 2014.
[2] B. Clive, D. I. R. Norris, C. Taylor and J. M. Titchmarsh, “Radiation-induced Segregation in 20Cr/25/Ni/Nb Stainless Steel,” in *Effects of Radiation on Materials: 15th International Symposium*, Philadelphia, 1992.
[3] D. I. R. Norris, C. Baker and J. M. Titchmarsh, “Compositional profiles at grain boundaries in 20%Cr/25%Ni/Nb stainless steel,” in *Radiation-induced segregation of stainless steels symposium*, 1986.
[4] S. M. Bruemmer, E. P. Simonen, P. M. Scott, P. L. Andresen and G. Was, “Radiation-induced Material Changes and Susceptibility to Intergranular Failure of Light Water Reactor Internals,” *Journal of Nuclear Materials,* vol. 274, no. 3, pp. 299-314, 1999.
[5] Z. Jiao and G. S. Was, “Novel Features of Radiation-induced Segregation and Radiation-induced Precipitation in Austenitic Stainless Steels,” *Acta Materialia,* vol. 59, pp. 1220-1238, 2011.
[6] C. S. Tedmon Jr., D. A. Vermilyea and J. H. Rosolowski, “Intergranular Corrosion of Austenitic Stainless Steel,” *Journal of the Electrochemical Society,* vol. 118, no. 2, pp. 192-202, 1971.
[7] S. J. Zinkle and G. S. Was, “Materials challenges in nuclear energy,” *Acta Materialia,* vol. 61, pp. 735-758, 2013.
[8] G. S. Was and T. Allen, “Radiation-induced segregation in multicomponent alloys: effect of particle type,” *Materials Characterization,* vol. 32, pp. 239-255, 1994.
[9] T. R. Allen and G. S. Was, “Modelling radiation-induced segregation in austenitic Fe-Cr-Ni alloys,” *Acta Metallurgica,* vol. 46, no. 10, pp. 3679-3691, 1998.
[10] E. C. Bain, R. H. Aborn and J. J. B. Rutherford, “The Nature and Prevention of Intergranular Corrosion in Austenitic Stainless Steels,” *American Society for Steel Treating,* vol. 21, pp. 481-509, 1933.
[11] D. I. R. Norris, C. Baker, C. Taylor and J. M. Titchmarsh, “Radiation-Induced Segregation in 20Cr/25Ni/Nb Stainless Steel,” *15th Symposium on Effects of Radiation on Materials,* 1990.
[12] D. Powell, R. Pilkington and D. A. Miller, “The precipitation characteristics of 20% Cr/25% Ni - Nb stabilised stainless steel,” *Acta Metallurgica,* vol. 36, no. 3, pp. 713-724, 1988.
[13] A. R. Jones and B. Ralph, “Growth and dissolution of NbC particles in an austenitic stainless steel,” *Metallography,* vol. 10, pp. 469-480, 1977.
[14] C. J. Moss and J. M. Sykes, “Thermal sensitisation of 20Cr/25Ni/Nb stainless steel,” in *Radiation-induced segregation of stainless steels symposium*, 1986.
[15] H. B. Aaron and H. I. Aaronson, “Growth of Grain Boundary Precipitates in Al-4% Cu by Interfacial Diffusion,” *Acta Metallurgica,* vol. 16, pp. 789-798, 1968.
[16] A. Iversen and B. Leffler, “3.04 Aqueous Corrosion of Stainless Steels,” in *Shreir's Corrosion*, ISBN: 978-0-444-52787-5 , 2010, pp. 1802-1878.
[17] A. F. Alshater, D. L. Engelberg, C. J. Donohoe, S. B. Lyon and A. H. Sherry, “Proton Irradiation Damage in Cold Worked Nb-stabilized 20Cr-25Ni Stainless Steel,” *Applied Surface Science,* vol. 454, no. https://doi.org/10.1016/j.apsusc.2018.05.128, pp. 130-137, 2018.
[18] C. Barcellini, R. W. Harrison, S. Dumbill, S. E. Donnelly and E. Jimenez-Melero, “Evolution of Radiation-induced Lattice Defects in 20/25 Nb-stabilised Austenitic Stainless

Steel during in-situ Proton Irradiation," *Journal of Nuclear Materials,* vol. 514, no. https://doi.org/10.1016/j.jnucmat.2018.11.019, pp. 90-100, 2019.
[19] C. Barcellini, R. W. Harrison, S. Dumbill, S. E. Donelly and E. Jimenez-Melero, "Local Chemical Instabilities in 20Cr-25Ni Nb-stabilised Austenitic Stainless Steel Induced by Proton Irradiation," *Journal of Nuclear Materials,* vol. 518, no. DOI: https://doi.org/10.1016/j.jnucmat.2019.02.035, pp. 95-107, 2019.
[20] C. Barcellini, S. Dumbill and E. Jimenez-Melero, "Isothermal Annealing Behaviour of Nuclear Grade 20Cr-25Ni Austenitic Stainless Steel," *Materials Characterisation,* vol. 145, no. https://doi.org/10.1016/j.matchar.2018.08.057, pp. 303-311, 2018.
[21] C. Barcellini, S. Dumbill and E. Jimenez-Melero, "Recrystallisation Behaviour of a Fully Austenitic Nb-stabilised Stainless Steel," *Journal of Microscopy,* vol. 274, no. 1, DOI: https://doi.org/10.1111/jmi.12776, pp. 3-12, 2019.
[22] S. Jiang, Thermally Induced Sensitisation of Austenitic Stainless Steel for AGR Fuel Cladding, University of Birmingham PhD Thesis: http://etheses.bham.ac.uk/id/eprint/9246, 2018.
[23] A. Laferrere, R. Burrows, C. Glover, O. Payton, L. Picco, S. Moore and G. Williams, "In-situ Imaging of Corrosion Processes in Nuclear Fuel Cladding," *Corrosion Engineering Science and Technology,* vol. 52, no. 8, pp. 596-604, 2017.
[24] A. F. Al-Shater, Intergranular Corrosion of Sensitized 20Cr-25Ni-Nb Stainless Steel Nuclear Fuel Cladding Materials, University of Manchester PhD Thesis: https://ethos.bl.uk/OrderDetails.do?uin=uk.bl.ethos.706485, 2010.
[25] J. Kyffin, "Spent Fuel Performance Assessment and Research. Final Report of a Coordinated Research Project on Spent Fuel Performance Assessment and Research (SPAR-III) 2009–2014: Corrosion Inhibition Studies in Support of the Long Term Storage of AGR Fuel," International Atomic Energy Authority, IAEA-TECDOC--1771, http://www-pub.iaea.org/MTCD/Publications/PDF/TE-1771_web.pdf;http://www.iaea.org/books, 2015.
[26] E. Howett, C. Boxall and D. Hambley, "AGR Cladding Corrosion: Investigation of the Effect of Temperature on Unsensitised Stainless Steel," in *Materials Research Society Advances*, https://doi.org/10.1557/adv.2016.651, 2016.
[27] A. Al-Shater, D. Engelberg, S. Lyon, C. Donohoe, W. S. Walters, G. Whillock and A. Sherry, "Characterization of the Stress Corrosion Cracking Behaviour of Thermally Sensitised 20Cr-25Ni Stainless Steel in a Simulated Cooling Pond Environment," *Journal of Nuclear Science and Technology,* vol. 54, no. 7, pp. 742-751, 2017.
[28] G. O. H. Whillock, B. J. Hands, T. P. Majchrowski and D. I. Hambley, "Investigation of Thermally Sensitised Stainless Steels as Analogues for Spent AGR Fuel Cladding to Test a Corrosion Inhibitor for Intergranular Stress Corrosion Cracking," *Journal of Nuclear Materials,* vol. 498, no. https://doi.org/10.1016/j.jnucmat.2017.10.017, pp. 187-198, 2018.
[29] W. S. Walters, P. Durham and N. A. Hodge, "The Adsorption and Desorption of Water from a Carbonaceous Deposit Layer on the Surface of Stainless Steel Representing Spent AGR Nuclear Fuel Cladding," *Journal of Nuclear Science and Technology,* vol. 55, no. 4; DOI: https://doi.org/10.1080/00223131.2017.1403384 , pp. 374-385, 2018.
[30] J. B. Goode, Transitioning of Spent Advanced Gas Reactor Fuel from Wet to Dry Storage, University of Leeds PhD Thesis: http://etheses.whiterose.ac.uk/id/eprint/20585, 2017.
[31] C. Anwyl, C. Boxall, R. Wilbraham, D. Hambley and C. Padovani, "Corrosion of AGR Fuel Pin Steel under Conditions Relevant to Permanent Disposal," *Procedia Chemistry,* vol. 21, no. https://doi.org/10.1016/j.proche.2016.10.035, pp. 247-254, 2016.

[32] C. H. Phuah, Corrosion of Thermally-aged Advanced Gas Reactor Fuel Cladding, Imperial College London PhD Thesis, 2012.
[33] C. M. Chan, D. L. Engelberg and W. S. Walters, “Performance Characterisation of AGR Fuel Cladding Relevant to Long-term in-pond Storage in pH-moderated Aqueous Environment,” in *Top Fuel* , 2015.
[34] M. Rohwerder and F. Turcu, “High-Resolution Kelvin Probe Microscopy in Corrosion Science: Scanning Kelvin Probe Force Microscopy (SKPFM) Versus Classical Scanning Kelvin Probe,” *Electrochimica Acta,* vol. 53, no. 2, pp. 290-299, 2007.
[35] G. Williams and H. N. McMurray, “Pitting Corrosion of Steam Turbine Blading Steels: The Influence of Chromium Content, Temperature, and Chloride Ion Concentration,” *Corrosion Science,* vol. 62, no. 3, pp. 231-242, 2006.
[36] G. Williams and H. N. McMurray, “Localised corrosion of magnesium in chloride-containing electrolyte studied by a scanning vibrating electrode technique,” *J. Electrochem Soc.,* vol. 155, no. 7, pp. C340-C349, 2008.
[37] L. Lacroix, L. Ressier, C. Blanc and G. Mankowski, “Combination of AFM, SKPFM, and SIMS to Study the Corrosion Behaviour of S-Phase Particles in AA2024-T351,” *Journal of the Electrochemical Society,* vol. 155, no. 4, p. C131, 2008.
[38] P. Schmutz and G. S. Frankel, “Corrosion Study of AA2024-T3 by Scanning Kelvin Probe Force Microscopy and In-Situ Atomic Force Microscopy Scratching,” *The Electrochemical Society,* vol. 145, no. 7, pp. 2295-2305, 1998.
[39] S. Riva, K. V. Yusenkoa, C. M. Fung, J. R. Searle, R. N. Clark and N. P. Lavery, “Formation and Disruption of W-Phase in High-Entropy Alloys,” *Metals,* vol. 106, no. 6, 2016.
[40] P. P. Lablanc and G. S. Frankel, “Investigation of Filiform Corrosion of Epoxy-Coated 1045 Carbon Steel by Scanning Kelvin Probe Force Microscopy,” *Journal of the Electrochemical Society,* vol. 151, no. 3, p. B105, 2004.
[41] E. Bettini, C. Leygraf, C. Lin, P. Liu and J. Pan, “Influence of Grain Boundaries on Dissolution Behaviour of Biomedical CoCrMo Alloy: In-Situ Electrochemical-Optical, AFM and SEM/TEM Studies,” *Journal of the Electrochemical Society,* vol. 159, pp. C422-C427, 2012.
[42] J. Sullivan, S. Mehraban and J. Elvins, “In-situ Monitoring of the Microstructural Corrosion Mechanisms of Zinc-magnesium-aluminium Alloys using Time-Lapse Microscopy,” *Corrosion Science,* vol. 53, no. 6, pp. 2208-2215, 2011.
[43] J. Sullivan, N. Cooze, C. Gallagher, T. Lewis, T. Prosek and D. Thierry, “In-situ Monitoring of Corrosion Mechanisms and Phosphate Inhibitor Surface Deposition during Corrosion of Zinc-magnesium-aluminium (ZMA) Alloys using Novel Time-Lapse Microscopy,” *Faraday Discussions,* vol. 180, pp. 361-379, 2015.
[44] R. N. Clark, Mapping of Corrosion Sites in Advanced Gas-cooled Reactor Fuel Cladding in Long Term Pond Storage, http://dx.doi.org/10.23889/SUthesis.40783: Swansea University PhD Thesis, 2018.
[45] T. L. Burnett, S. A. McDonald, A. Gholinia, R. Geurts, M. Janus, T. Slater, S. J. Haigh, C. Ornek, F. Almuaili, D. L. Engelberg, G. E. Thompson and P. J. Withers, “Correlative Tomography,” *Scientific Reports,* p. 4711, 2014.
[46] M. P. Ryan, N. J. Laycock, H. S. Isaacs and R. C. Newman, “Corrosion Pits in Thin Films of Stainless Steel,” *Journal of the Electrochemical Society,* vol. 146, no. 1, p. 91, 1999.
[47] N. J. Laycock, S. P. White, J. S. Noh, P. T. Wilson and R. C. Newman, “Perforated Covers for Propagating Pits,” *Journal of the Electrochemical Society,* vol. 145, p. 1101, 1998.

[48] R. C. Newman, “Understanding the Corrosion of Stainless Steel,” *Corrosion,* vol. 57, no. 12, pp. 1030-1041, 2001.
[49] H. S. Issacs and B. Vyas, “Scanning Reference Electrode Techniques in Localised Corrosion,” Brookhaven National Laboratory, BNL-26094, 1979.
[50] S. Moore, R. Burrows, L. Picco, T. L. Martin, S. J. Greenwell, T. B. Scott and O. D. Payton, “A Study of Dynamic Nanoscale Corrosion Initiation Events using HS-AFM,” *Faraday Discussions,* vol. 210, pp. 409-428, 2018.
[51] G. Bai, S. Lu, D. Li and Y. Li, “Influences of niobium and solution treatment temperature on pitting corrosion behaviour of stabilised austenititc stainless steels,” *Corrosion Science,* vol. 108, pp. 111-124, 2016.
[52] C. -O. Olsson and D. Landolt, “Passive Films on Stainless Steels - Chemistry, Structure and Growth,” *Electrochimica Acta,* vol. 48, pp. 1093-1104, 2003.
[53] R. F. A. Jargelius-Pettersson, “Electrochemical Investigation of the Influence of Nitrogen Alloying on Pitting Corrosion of Austenitic Stainless Steels,” *Corrosion Science,* vol. 41, no. 8, pp. 1639-1664, 1999.
[54] Q. Zhang, R. Wang, M. Kato and K. Nakasa, “Observation by Atomic Force Microscope of Corrosion Product during Pitting Corrosion on SUS304 Stainless Steel,” *Scripta Materialia,* vol. 52, pp. 227-230, 2005.
[55] M. Ryan, D. E. Williams and R. Chater, “Why Stainless Steel Corrodes,” *Nature,* vol. 415, pp. 770-774, 2002.
[56] E. Maire and P. J. Withers, “Quantitative X-ray Tomography,” *International Materials Reviews,* vol. 59, no. 1, DOI: https://doi.org/10.1179/1743280413Y.0000000023, pp. 1-43, 2014.
[57] S. M. Ghahari, A. J. Davenport, T. Rayment, T. Suter, J.-P. Tinnes, C. Padovani, J. A. Hammons, M. Stampanoni, F. Marone and R. Mokso, “In Situ Synchrotron X-ray Micro-tomography Study of Pitting Corrosion in Stainless Steel,” *Corrosion Science,* vol. 53, no. DOI: https://doi.org/10.1016/j.corsci.2011.05.040, pp. 2684-2687, 2011.
[58] L. M. Picco, L. Bozec, A. Ulcinas, D. J. Engledew, M. Antognozzi, M. A. Horton and M. J. Miles, “Breaking the Speed Limit with Atomic Force Microscopy,” *Nanotechnology,* vol. 18, 2006.
[59] J. Takahashi, K. Kawakami, J.-i. Hamada and K. Kimura, “Direct observation of niobium segregation to dislocations in steel,” *Acta Materialia,* vol. 107, pp. 415-422, 2016.
[60] T. Ando, “High-speed Atomic Force Microscopy,” *Microscopy,* vol. 62, no. 1 DOI: https://doi.org/10.1093/jmicro/dfs093, pp. 81-93, 2013.

Figure Captions:

Figure 1: AFM (left) and SKPFM (right) maps of the as-received 20Cr-25Ni-Nb microstructure showing NbC inclusions and grain boundaries.

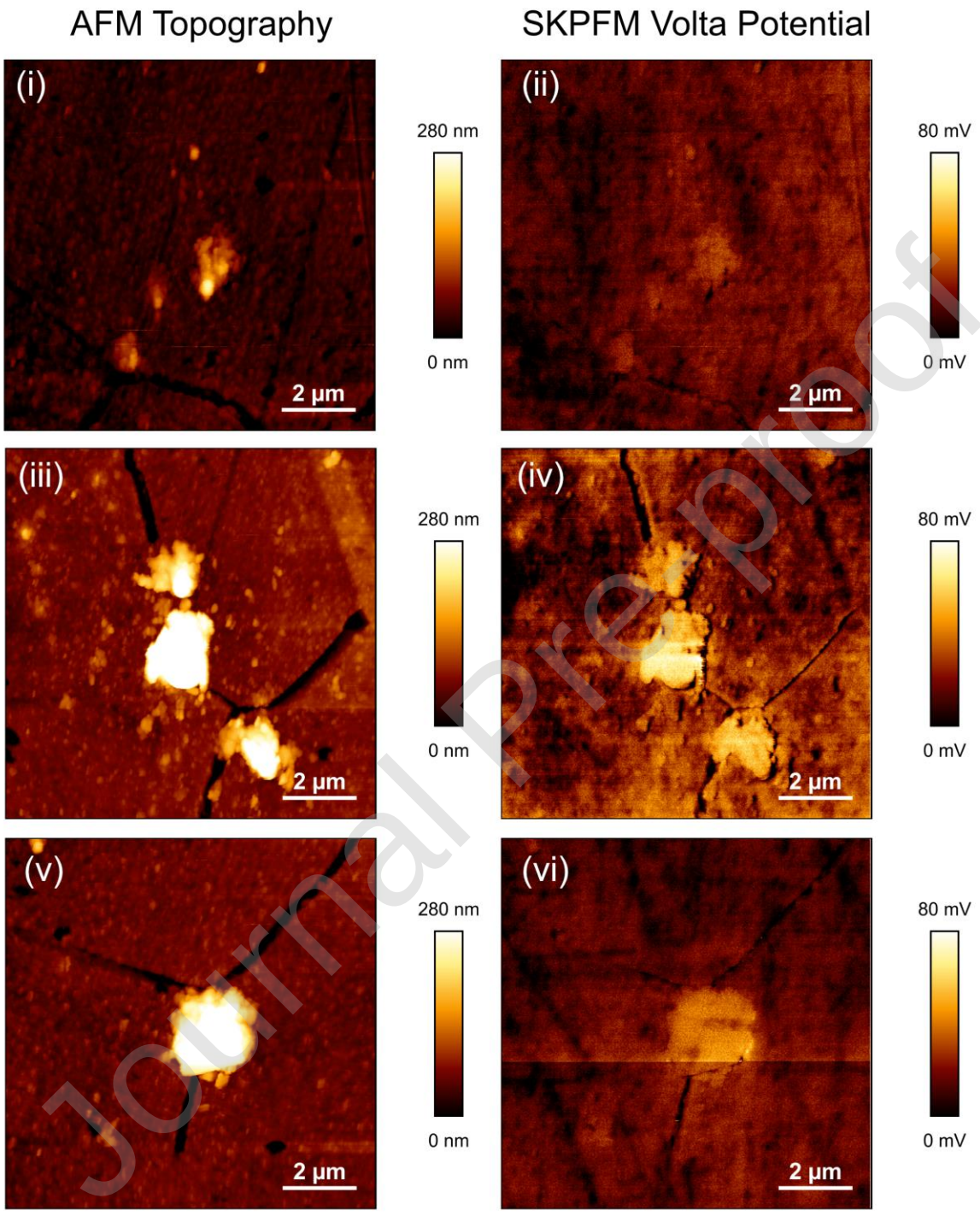

Figure 2: Backscatter SEM image of the thermally sensitised microstructure, annotated to show the location of Cr carbides and NbC inclusions.

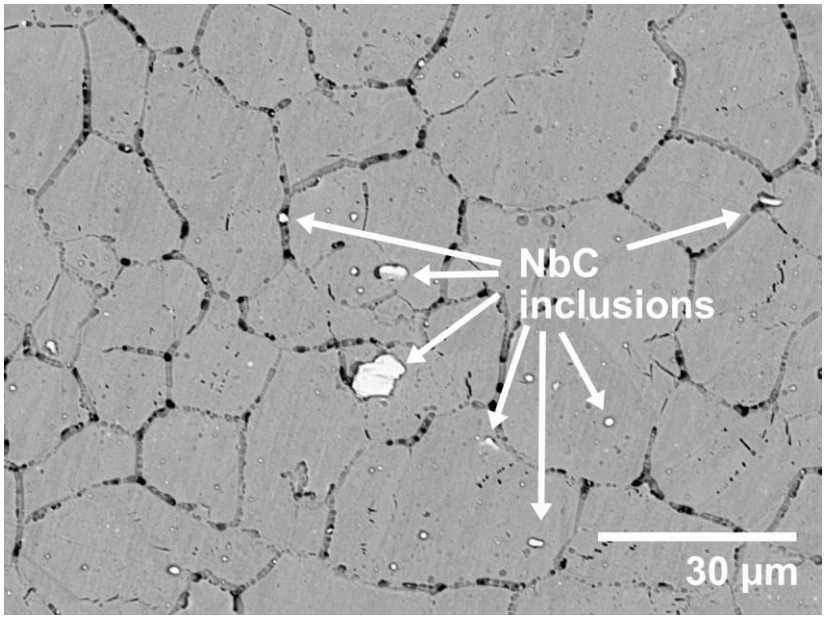

Figure 3: AFM (left) and SKPFM (right) maps of the thermally sensitised 20Cr-25Ni-Nb microstructure showing Cr carbide precipitates and sensitised grain boundaries.

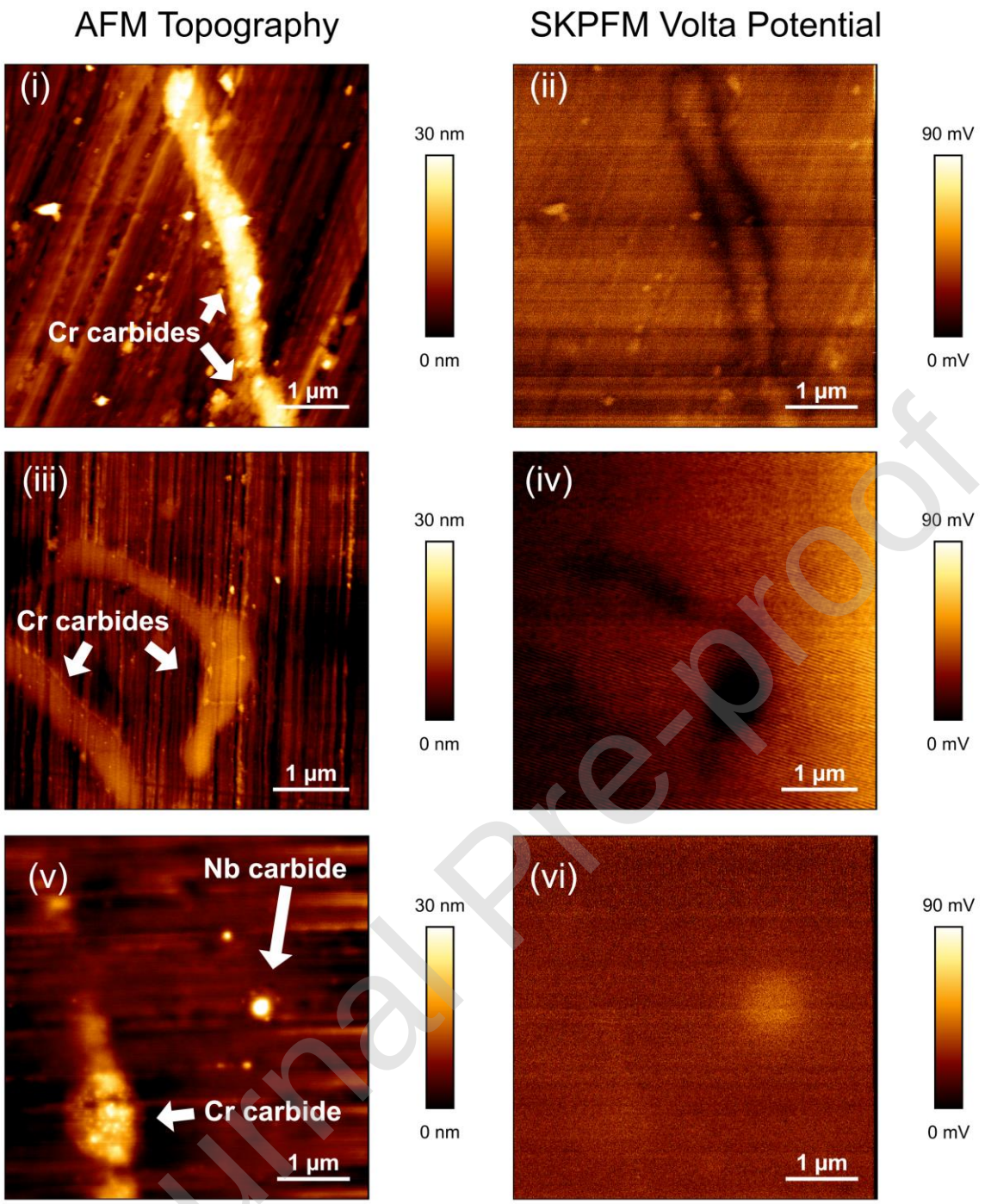

Figure 4: Time-lapse microscopy stills of thermally sensitised 20Cr-25Ni-Nb under potentiodynamic polarisation at breakdown potential.

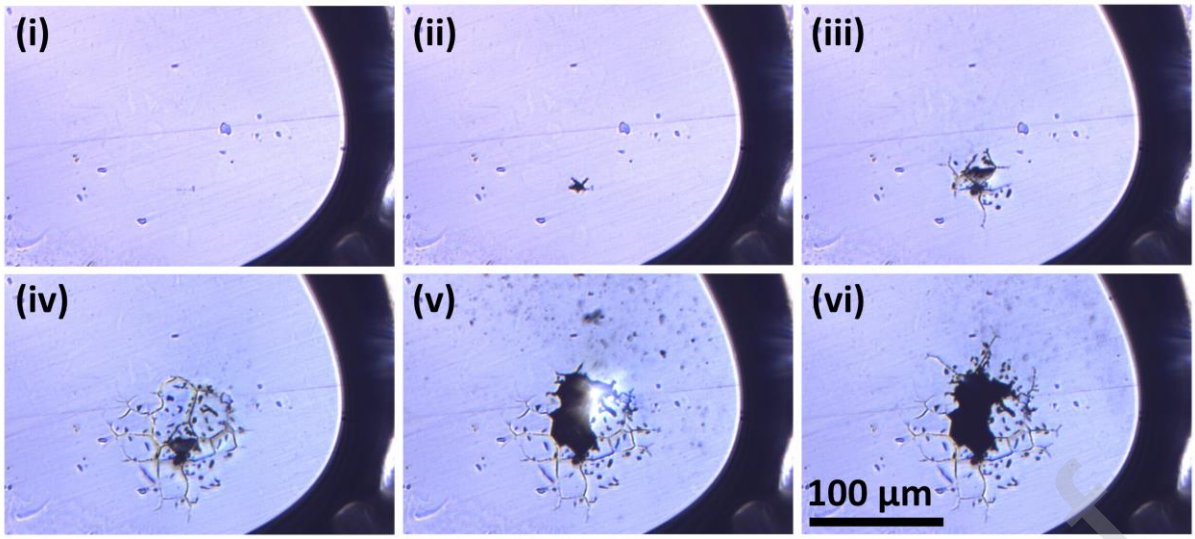

Figure 5: Cropped images of the stills recorded from the time-lapse microscopy experiment. The red arrow shows the location of an NbC inclusion, which remained unaffected during the experiment.

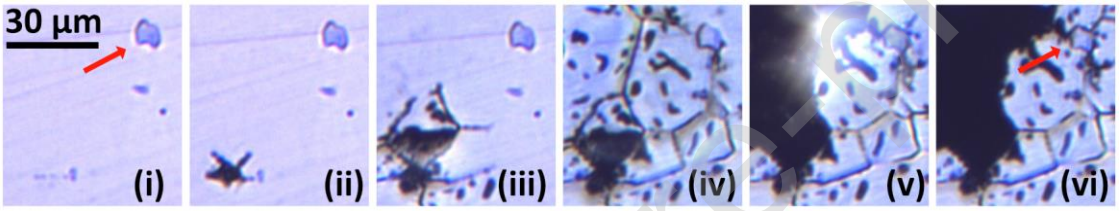

Figure 6: (i-vi) SVET current density maps of thermally sensitised 20Cr-25Ni-Nb obtained in 1 $g{\cdot}L^{-1}$ NaCl (aq) at 700, 750, 800 mV_{SCE}. The green line in (ii) shows the location of the cross section in Figure 7, and each pit site is labelled A-G.

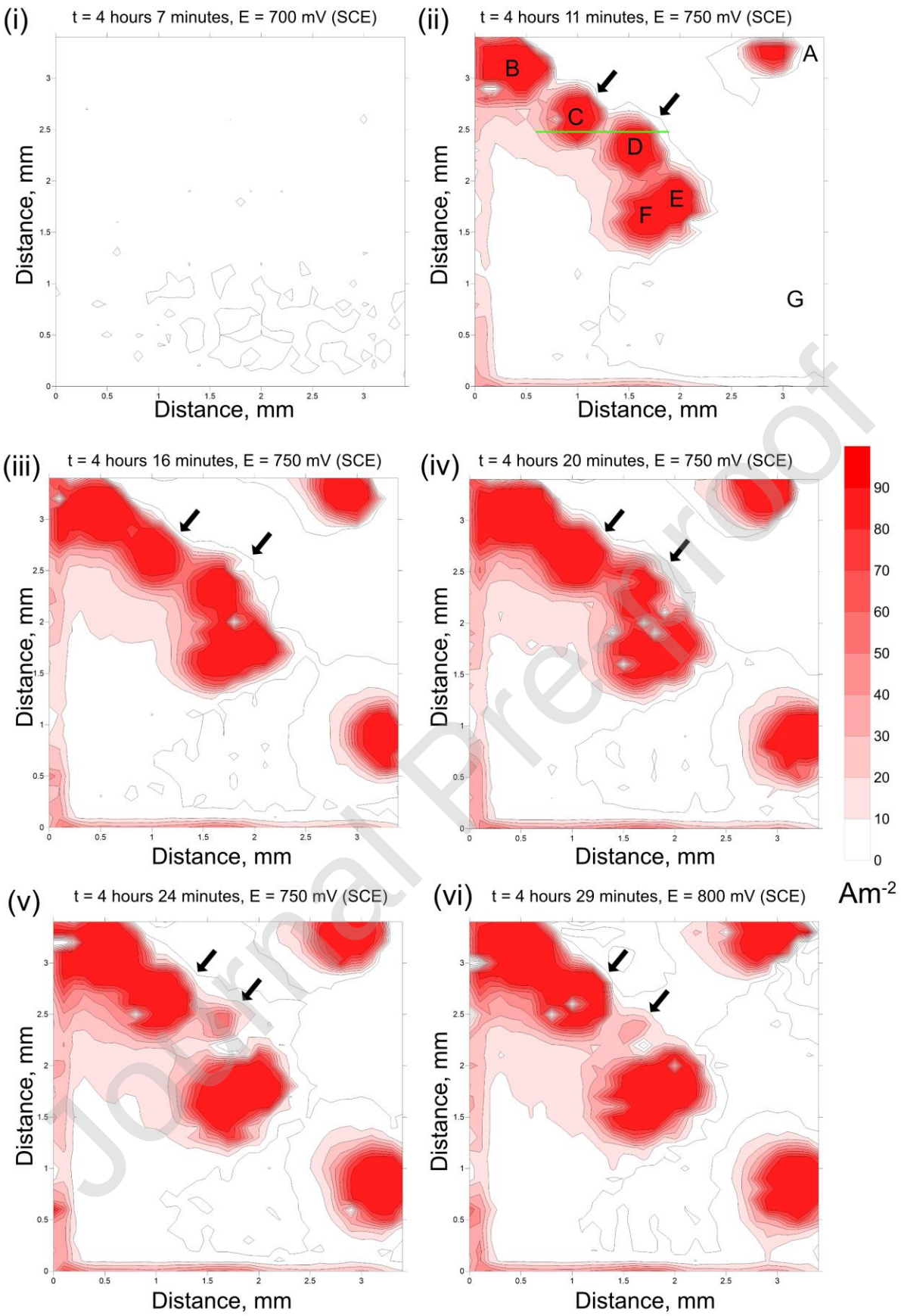

Figure 7: Line profiles as a function of time showing the evolution in current density for two competitive anodes and estimates for current density for 4h 11m and 4h 16m. Site C is located on the left, which shows an increasing trend toward higher current densities, and site D on the right, which shows a corresponding decay in current density.

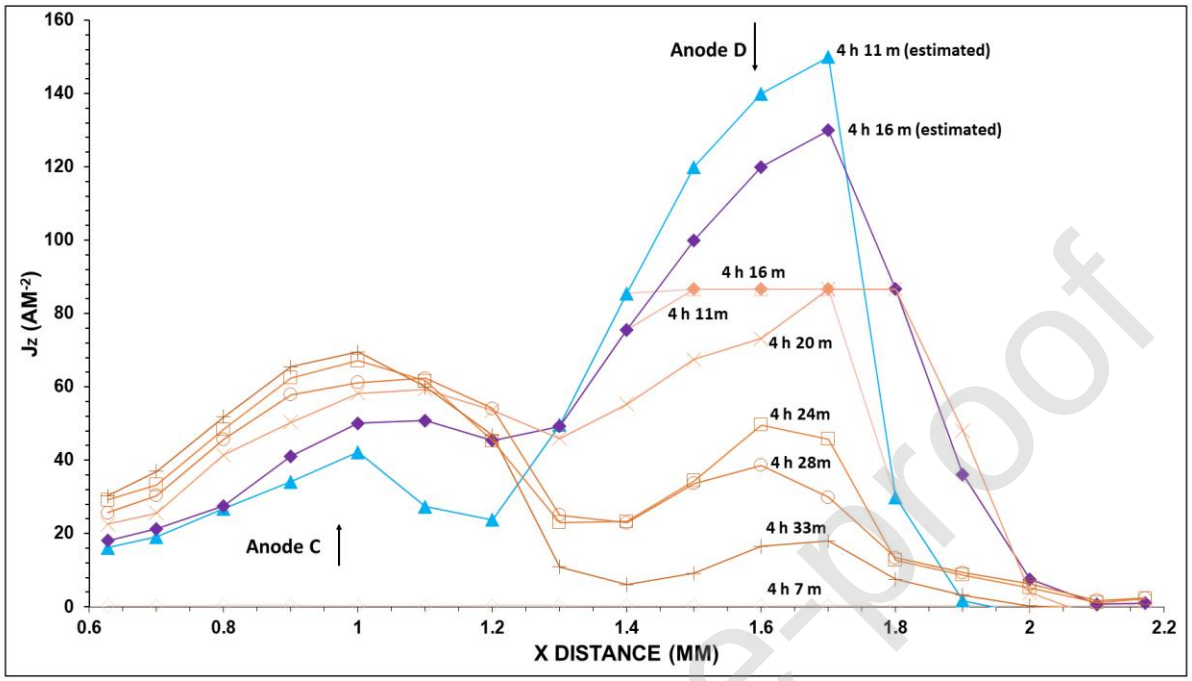

Figure 8: (i, iii) Backscatter SEM images of the intergranular pit at anode site B at different magnifications. The red arrows highlight locations where Cr carbides have been removed from grain boundaries. (ii, iv) corresponding Nb EDS false colour maps of the same locations.

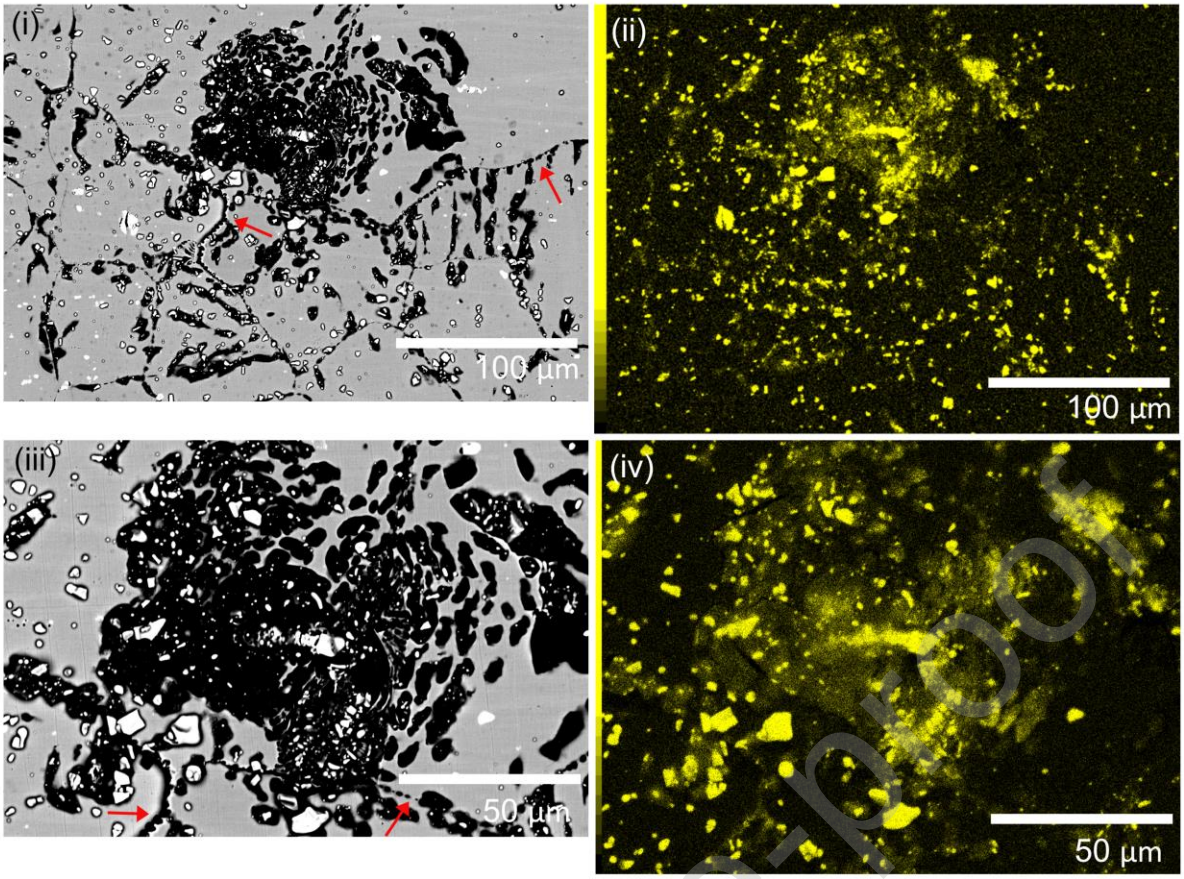

Figure 9: (i) Backscatter SEM images of the intergranular pit at anode site D and (ii) corresponding EDS false colour map. The red arrows show the presence of Nb located along a grain boundary.

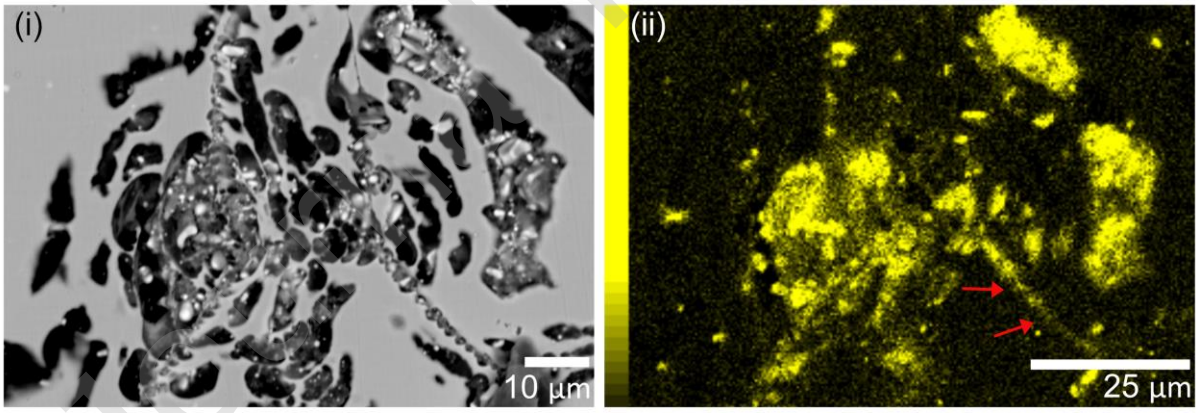

Figure 10: (i) Backscatter SEM images of the intergranular pit at anode site G. The green arrow corresponds to the image in (ii), showing blocky NbC inclusions present within the pit. The purple arrow corresponds to the image in (iii) showing the abundance of Nb-rich inclusions present at the intergranular pit; red arrows show locations where Cr carbides have been removed from the grain boundaries. (iv) EDS Nb false colour map of the area in (iii).

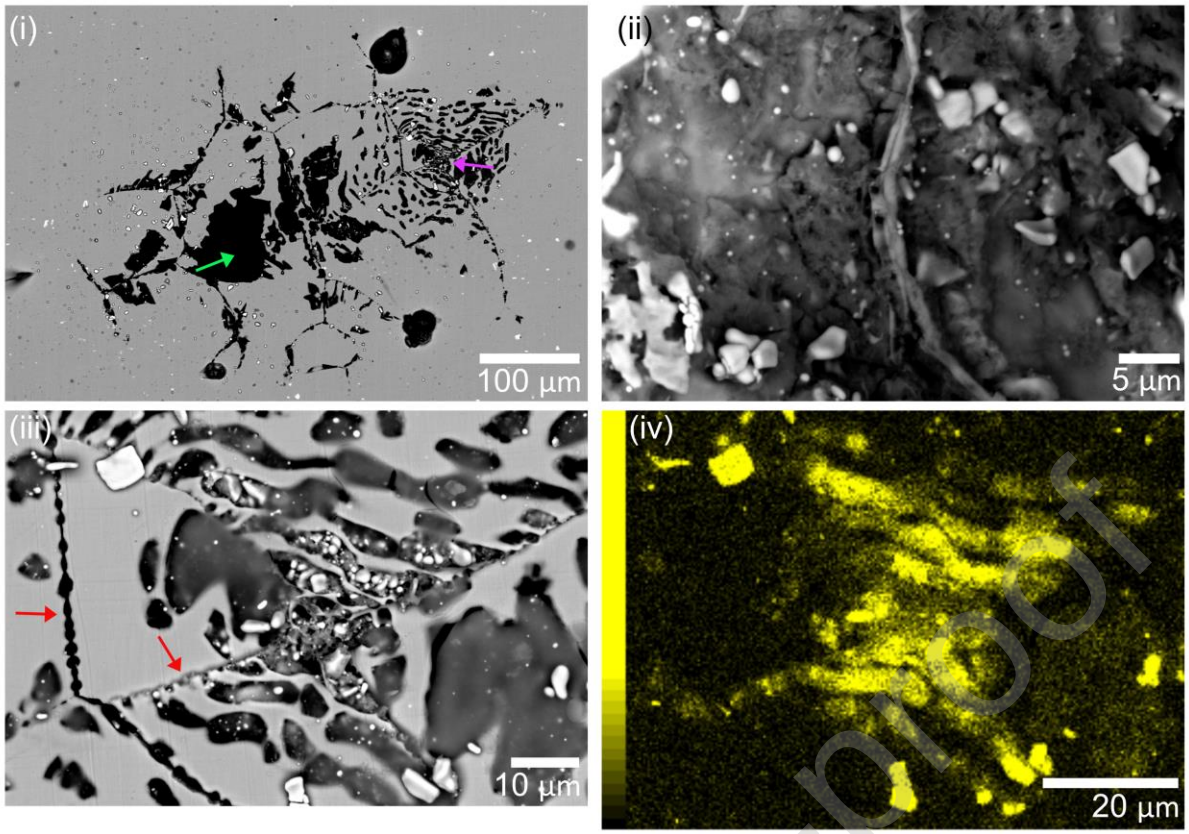

Figure 11: Post corrosion secondary electron SEM images of (left) an intergranular pit following removal of the lacy cover, showing the presence of blocky NbC inclusions of varying shape and size. The area highlighted by the arrow, an oxidised grain boundary, is shown in (ii).

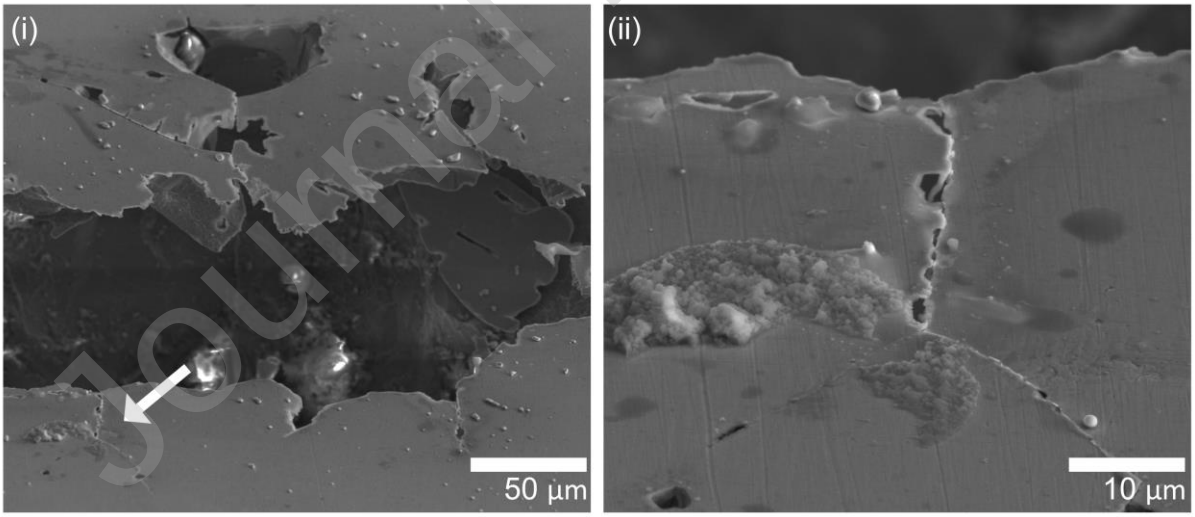

Figure 12: Secondary electron SEM imaging of Nb-rich inclusion (i) before, and (ii) after FIB sectioning along an oxidised grain boundary. (iii) Higher magnification secondary electron SEM imaging of the Nb-rich inclusion, EDS spectra of: (iv) the matrix and (v) the inclusion.

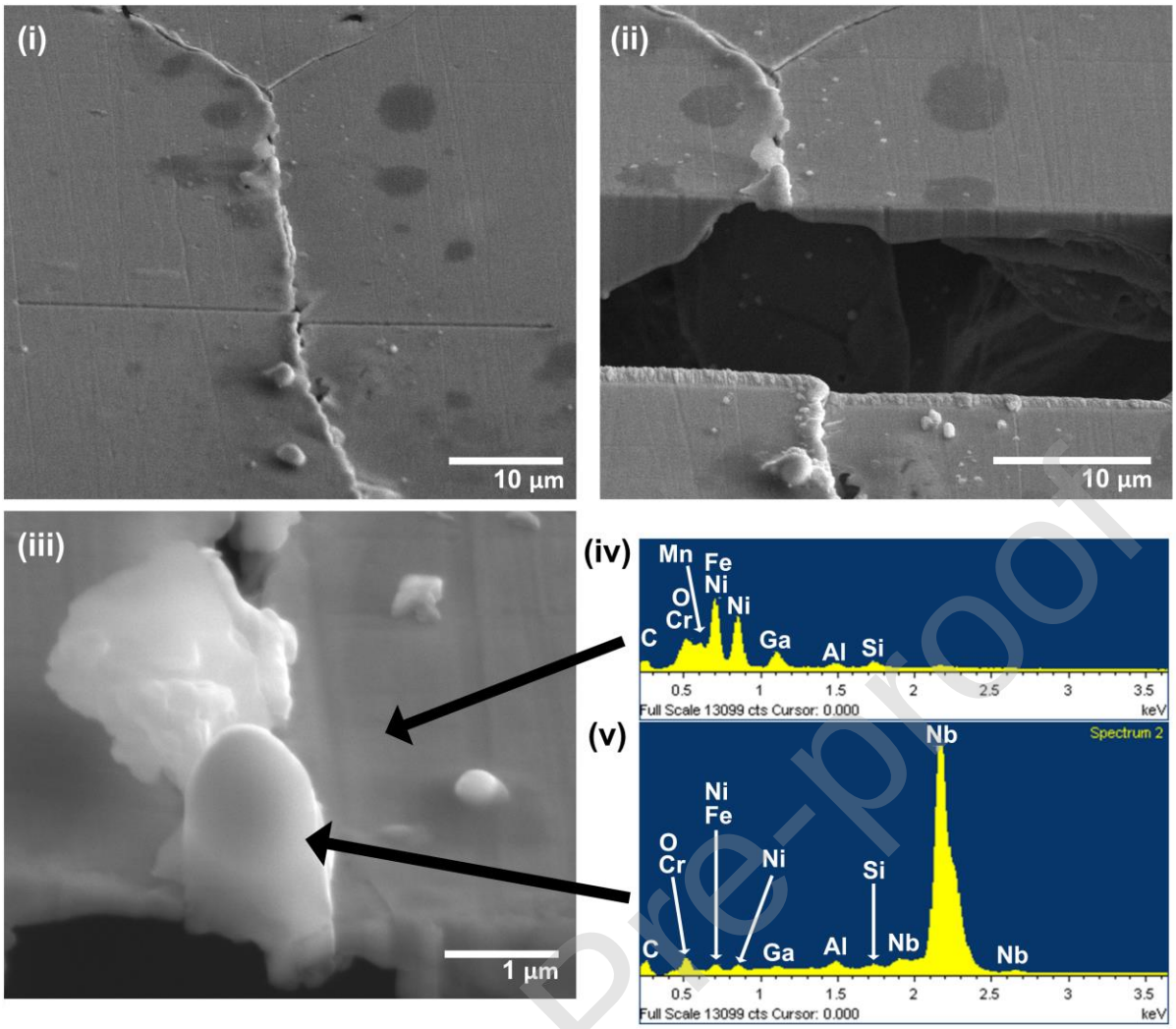

Figure 13: Electrochemical atomic force microscopy stills of the *in-situ* time lapse experiment, showing the initiation, and propagation of pits on a sensitised 20Cr-25Ni-Nb specimen scans (i) 30 minutes, (ii) 1 hour, (iii) 1 hours 30 minutes, (iv) 2 hours, (v) 2 hours 30 minutes, (vi) 4 hours.

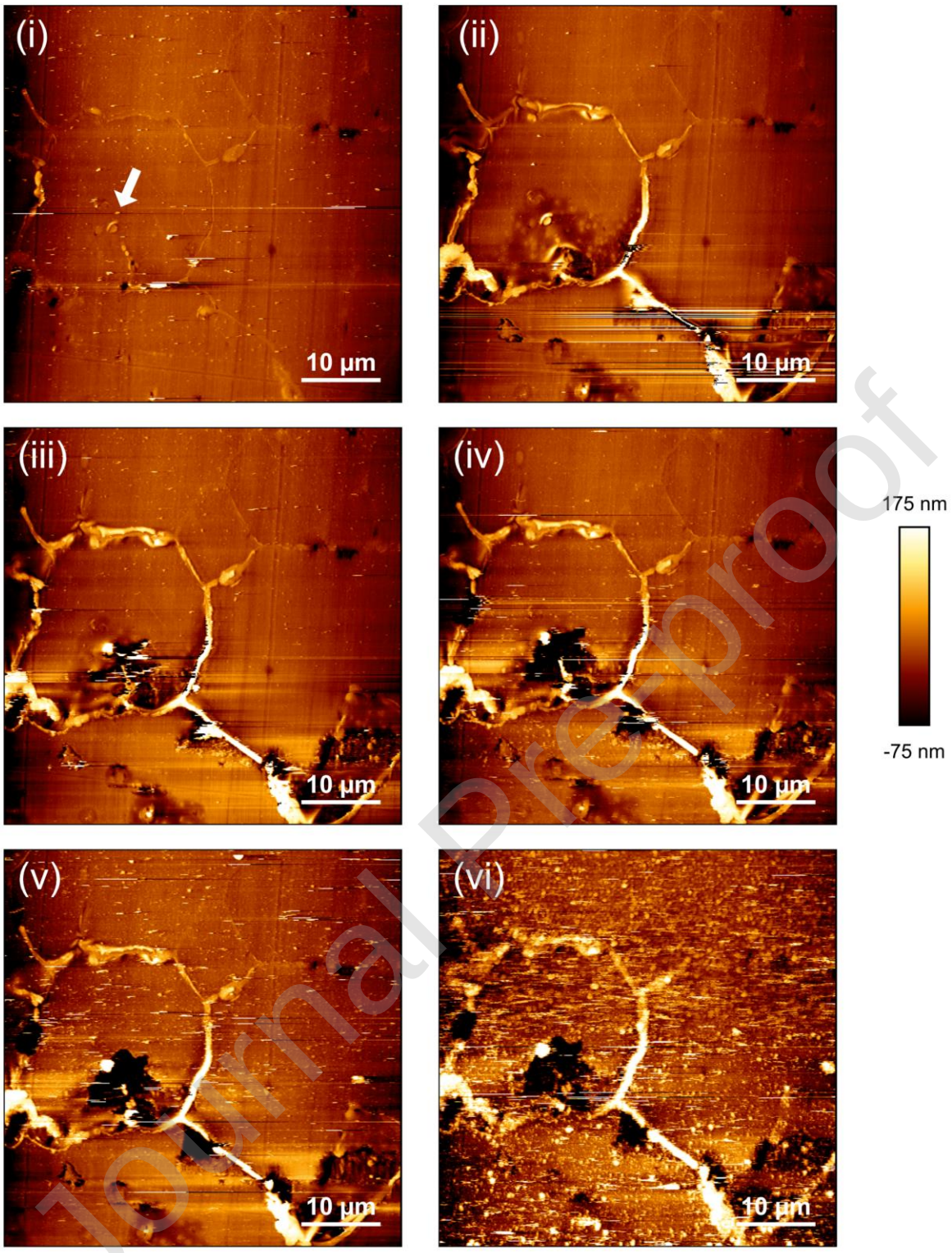

Figure 14: Backscatter SEM images of pits formed on unsensitised 20Cr-25Ni-Nb following a potentiodynamic polarisation experiment in 0.35 $g \cdot L^{-1}$ [Cl^-]. The arrows highlight the presence of NbC inclusions at pit sites.

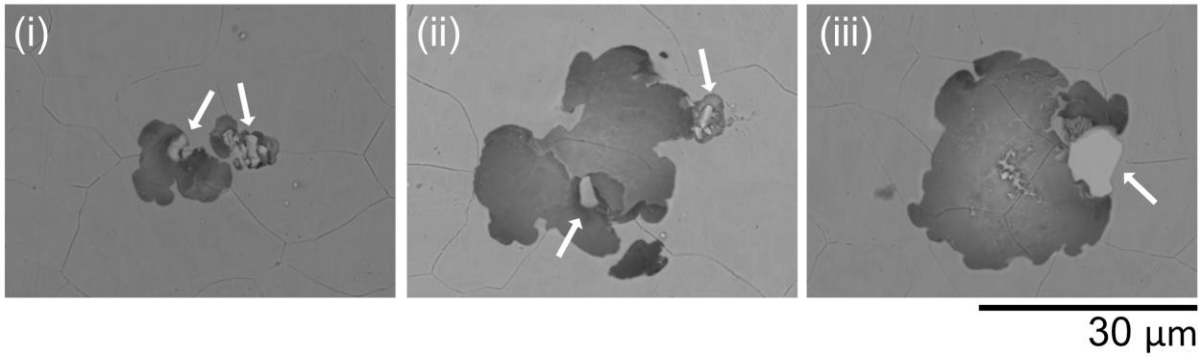

Tables:

Table 1: Typical 20Cr-25Ni-Nb stainless steel composition in weight %, from [27].

% Fe	% Cr	% Ni	% Nb	% Si	% Mn	% Ti	% C
Balance	**19.9**	**24.5**	**0.64**	**0.57**	**0.72**	**0.014**	**0.055**

Table 2: Overview of experimental conditions

Experiment	**Technique**	**Environment**	**Approximate length scale**
Determination of phases susceptible to corrosion	AFM / SKPFM	Air, electrolytic etch used to reveal microstructure, no polarisation	100 nm – 10s of µm
Identification of anodic and cathodic corrosion sites *in-situ*	SVET[2] / SEM-EDS[3] / FIB-SEM[4]	1 $g \cdot L^{-1}$ [Cl^-], potentiostatic polarisation	100 µm – 10s of mm
Mapping corrosion sites *in-situ* on the microstructural length scale	TLM[5] / SEM	0.35 $g \cdot L^{-1}$ [Cl^-], potentiodynamic polarisation	10s µm – 200 µm
High magnification *in-situ* corrosion site mapping	EC-AFM[6]	35.5 $g \cdot L^{-1}$ [Cl^-], no polarisation	100 nm – 10s of µm

[2] SVET – scanning vibrating electrode technique
[3] SEM-EDS - scanning electron microscopy energy dispersive X-ray spectroscopy
[4] FIB-SEM – focussed ion beam scanning electron microscopy
[5] TLM – time lapse microscopy
[6] EC-AFM – electrochemical atomic force microscopy